Epitaxial growth and properties of cobalt-doped ZnO on α-Al_2O_3 single-crystal substrates

A. C. Tuan,[1] J. D. Bryan,[2] A. B. Pakhomov,[3] V. Shutthanandan,[4] S. Thevuthasan,[4] D. E. McCready,[4] D. Gaspar,[4] M. H. Engelhard,[4] J. W. Rogers, Jr.,[4] K. Krishnan,[3] D. R. Gamelin,[2] and S. A. Chambers[5,*]

[1]*Department of Chemical Engineering, University of Washington, Seattle, Washington, USA*

[2]*Department of Chemistry, University of Washington, Seattle, Washington, USA*

[3]*Department of Materials Science and Engineering, University of Washington, Seattle, Washington, USA*

[4]*Environmental Molecular Sciences Laboratory, Pacific Northwest National Laboratory, Richland, Washington 99352, USA*

[5]*Fundamental Science Directorate, Pacific Northwest National Laboratory, Richland, Washington 99352, USA*

(Received 19 August 2003; revised manuscript received 21 May 2004; published 30 August 2004)

Co-doped ZnO($Co_xZn_{1-x}O$) is of potential interest for spintronics due to the prediction of room-temperature ferromagnetism. We have grown epitaxial $Co_xZn_{1-x}O$ films on Al_2O_3(012) substrates by metalorganic chemical vapor deposition using a liquid precursor delivery system. High concentrations of Co($x \leqslant 0.35$) can be uniformly incorporated into the film without phase segregation. Co is found to be in the +2 oxidation state, independent of x, by both surface-sensitive core-level x-ray photoemission and bulk-sensitive optical absorption spectroscopies. This material can be grown n-type by the deliberate incorporation of oxygen vacancies, but not by inclusion of ~1 at. % Al. Semiconducting films remain ferromagnetic up to 350 K. In contrast films without oxygen vacancies are insulating and nonmagnetic, suggesting that exchange interaction is mediated by itinerant carriers. The saturation and remanent magnetization on a per Co basis was very small ($<0.1\ \mu_B$/Co), even in the best films. The dependence of saturation magnetization, as measured by optical magnetic circular dichroism, on magnetic field and temperature, agrees with the theoretical Brillouin function, demonstrating that the majority of the Co(II) ions behave as magnetically isolated $S=3/2$ ions.

DOI: 10.1103/PhysRevB.70.054424 PACS number(s): 73.61.Le

I. INTRODUCTION

With silicon-based electronics approaching fundamental fabrication and performance limits, the use of quantum mechanical spin states in semiconductor devices represents an exciting new concept. For example, the additional degree of freedom provided by spin would enable the development of spin-transistors, high performance nonvolatile memories, and polarized light emitting devices. In the emerging field of quantum computing and communication, the electron spin is a natural candidate for the qubit–the fundamental unit of quantum information.[1] Loss and Vincenzo show that these spin qubits, when located in quantum-confined structures, satisfy all the requirements for a scalable quantum computer.[2] These quantum-confined structures include semiconductor quantum wells and quantum dots with a wide range of dimensions. The common goal of both analog and digital spintronics is to gain control over and effectively utilize the dynamics of spins in semiconductor device structures.

Ferromagnetism provides an ideal way to achieve the spin polarization necessary for realization of spintronic technologies, provided the spin injection material remains ferromagnetic at or above room temperature *and* is capable of high efficiency spin injection into semiconductor heterostructures. Given these requirements, ferromagnetic metals are very attractive because they have Curie temperatures that are well above room temperature. However, ferromagnetic metals are typically inefficient spin injectors, exhibiting spin injection efficiencies on the order of ~1%.[3] This low efficiency is due to the sizeable conductivity mismatch that exists at the metal-semiconductor interface. A simple resistor model has been proposed to explain this phenomenon and reveals that the spin polarization is proportional to the ratio of the resistances in the metal and the semiconductor. One way to circumvent the conductivity mismatch issue has been shown experimentally by Hanbicki *et al.*[4] By using an insulating AlGaAs Schottky barrier between Fe and a GaAs-AlGaAs quantum well structure, these workers demonstrated ~30% spin injection efficiency at room temperature.

A superior approach, in principle, is to use a diluted magnetic semiconductor (DMS) whose conductivity has been tuned (by altering the dopant level) to match that of the channel material. For example, $Be_yMn_xZn_{1-x-y}Se$ and (Mn,Zn)Se have been utilized as efficient spin injectors, with spin polarizations between 40% and 50%, into (Al,Ga)As-GaAs-(Al,Ga)As quantum well structures.[5,6] However, these materials are Brillouin paramagnets, and the spin polarization effect can be maintained only with an external magnetic field. Thus, DMS materials that are strongly ferromagnetic at and above room temperature are highly desirable. Indeed, a few unconventional semiconductors have exhibited room temperature ferromagnetism. These include $Mn_xGa_{1-x}N$,[7] $Co_xTi_{1-x}O_2$,[8] and $Co_xZn_{1-x}O$.[9]

Interest in ZnO-based DMSs was initially generated by the theoretical work of Dietl and coworkers. Their calculations showed that both Mn-doped ZnO and Mn-doped GaN would exhibit above-room-temperature ferromagnetism if the materials were grown with substitutional Mn^{+2} ions and sufficiently high levels of some p-type dopant (~3×10^{20} atoms/cm^3).[10] Recently, Mn-doped GaN films with Curie temperatures greater than 300 K have been synthesized,[7] while Mn-doped ZnO has been shown to be ferromagnetic with a Curie temperature of 250 K.[11]

Ab initio calculations by Sato *et al.* indicated that *n*-type Co-doped ZnO would remain ferromagnetic above room temperature as well.[12] Subsequent experiments, performed by Ueda *et al.*, showed ferromagnetism up to 320 K; however, the reproducibility was less than 10%.[9]

In this paper, we describe the plasma-enhanced metalorganic chemical vapor deposition (MOCVD) of epitaxial, Al-doped $Co_xZn_{1-x}O(110)$ on $Al_2O_3(012)$ using a liquid precursor delivery system. These MOCVD-grown films consistently show weak ferromagnetism with a Curie temperature of at least 350 K, which is the highest temperature measured to date for doped ZnO. The Co ions are in the +2 oxidation state and there is no evidence for the formation of metallic Co or CoO_x clusters. We show that the magnetic properties depend critically on the conductivity, which is greatly improved by vacuum annealing since oxygen vacancies, not aluminum dopants, have been found to be the source of the *n*-type conductivity. Finally, low-temperature electronic absorption and magnetic circular dichroism (MCD) data are presented from which we have identified and assigned a subbandgap charge transfer transition. The presence of such a transition is of relevance to the functional properties of this material as it reveals covalent mixing between the dopant ion and the semiconductor wave functions, which is important for ferromagnetism.

II. EXPERIMENT

Film deposition was performed in an Emcore Discovery 75 metalorganic chemical vapor deposition reactor, modified to incorporate a 1.5 kW downstream microwave source (ASTeX, AX7610) and a multi-wavelength spectroscopic ellipsometer (J. A. Woollam, M44). The system is a cold-wall, vertical, stainless steel reactor in which substrates are mounted on a high-speed rotating disk (up to 2000 rpm). Oxygen is supplied through a quartz tube that is located a half inch above the substrate surface, which minimizes gas-phase reactions. The substrate heater consists of a heating filament, located approximately 3 mm below the susceptor, which enables substrates to reach a maximum temperature of 1000°C. The substrate temperature was measured using a type-R thermocouple positioned approximately 0.8 mm below the susceptor. As a calibration, the surface temperature of a silicon substrate mounted on the susceptor was measured directly using a two-color infra-red pyrometer, and was found to be approximately 20°C higher than the thermocouple value near the growth temperature, which was typically 475°C. In order to prevent the introduction of moisture into the reactor and reduce substrate surface contamination by airborne particles, samples were introduced into the growth chamber through a quick-access door that is enclosed in a nitrogen ambient glove box.

The system is equipped with two metalorganic precursor delivery systems–(i) three bubblers with heated vapor delivery lines, and (ii) a direct liquid-source injection system (ATMI, LDS-300B) with two source reservoirs. The liquid delivery system is especially well-suited for oxide thin film growth and addresses specific precursor delivery challenges including low vapor pressure liquid-solid precursors, condensation of source material in nonuniformly heated delivery lines, and poor precursor mixing in multi-component materials. The liquid-delivery system operates by flash vaporizing the precursors (typically at 230°C) immediately prior to delivery by argon carrier gas into the growth chamber.

TABLE I. Summary of MOCVD growth parameters.

Substrate temperature	300–650°C
Chamber pressure	40 Torr
Oxygen flow rate	80–120 sccm
Liquid precursor flow rate (total)	0.08–0.15 mL/min
Carrier gas flow rate through TEAl	0–30 sccm
Sample rotation rate	600 rpm
Microwave plasma power	0–600 Watts
Growth rate	15–90 minutes
Film thickness	400–6000 Å

The zinc and cobalt sources were both β-diketonate based, solid precursors Bis(2,2,6,6-tetramethyl-3,5-heptanedionato) zinc $[Zn(tmhd)_2]$, and $Co(tmhd)_3$. The Zn and the Co precursors were initially dissolved in separate bubblers and then diluted in a 75% tetrahydrofuran/25% isopropanol solvent mixture to 0.14 and 0.05 M, respectively. The isopropanol was added in order to increase the boiling point of the solvent to prevent premature vaporization during precursor delivery. Altering the volume ratio between the two precursor solutions changes the Zn to Co ratio in the solution, and therefore alters the film composition.

Triethylaluminum (TEAl) was chosen over the more common trimethylaluminum (TMAl) because TMAl is prone to introduce carbon contamination due to the strong aluminum-carbon bond.[13] The vapor pressure, as a function of temperature, for TEAl is given by the following:

$$\log_{10}P = 8.99 - \left[\frac{2361.2}{T - 73.82}\right], \tag{1}$$

where P is in units of Torr, and T is the temperature of the bubbler in units of Kelvin. The bubbler was kept at room temperature, where the vapor pressure was 29 mTorr, and argon was used as a carrier gas to deliver the TEAl to the chamber. The TEAl flowed through a line heated to ~100°C and kept separate from the Co and Zn sources to prevent condensation and premature mixing.

Films were deposited on $Al_2O_3(012)$ single crystals, which is commonly referred to as *r*-plane sapphire. Prior to growth, the substrates were degreased by sonicating first in acetone for five minutes and then in isopropanol for five minutes. The substrates were then immediately loaded into the reactor and heated to the growth temperature (typically 475°C) in an oxygen plasma to remove any residual carbon contamination from the surface. Film growth was initiated after the substrate had been heated for ~5 min at the growth temperature. The specific processing parameters during film synthesis are summarized in Table I. After deposition, the $Co_xZn_{1-x}O$ films were cooled to room temperature in a flowing O_2-Ar gas mixture.

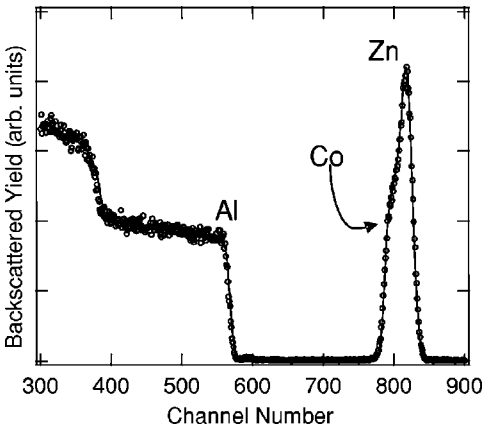

FIG. 1. RBS data (circles) for a $Co_xZn_{1-x}O$ where x has been shown to be 0.35 by quantitative analysis (solid line).

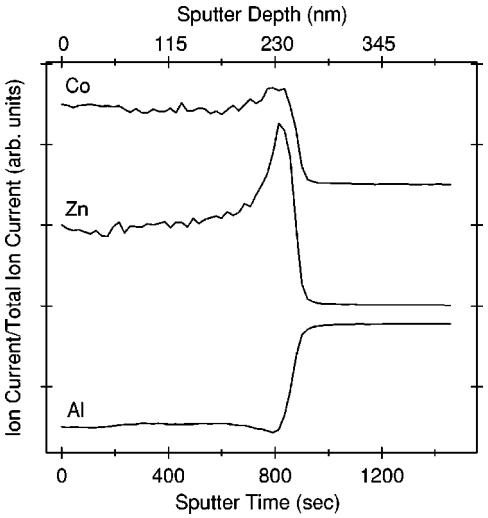

FIG. 2. Co, Zn, and Al SIMS depth profiles for a $Co_{0.09}Zn_{0.91}O$ film with ~1% Al-doping.

In order to explore the effects of post-growth vacuum annealing, samples were loaded into a vacuum chamber with a base pressure of 2×10^{-10} Torr. Immediately prior to annealing, each sample was heated to 150 °C and cleaned in an oxygen plasma for ~15 min at an oxygen partial pressure of 2×10^{-5} Torr. The $Co_xZn_{1-x}O$ films were then annealed at 500 °C for 20 min in vacuum and then allowed to cool to room temperature.

The films were characterized by various *ex situ* techniques. X-ray photoelectron spectroscopy (XPS), Rutherford backscattering spectrometry (RBS), and secondary ion mass spectrometry (SIMS) were used to determine the film composition. The film structure and surface morphology were characterized by x-ray diffraction (XRD) and atomic force microscopy (AFM), respectively. The electrical properties, including resistivity, carrier concentration, and carrier mobility, were determined by four-point probe resistance and Hall measurements. The magnetic properties of the film were characterized using a vibrating sample magnetometer (VSM), and a temperature-dependent superconducting quantum interference device (SQUID). Electronic absorption spectra were obtained using a Cary 500 UV-VIS-NIR spectrophotometer fitted with a closed cycle He cryostat. Magnetic circular dichroism (MCD) spectra were collected using an Aviv 40DS circular dichroism spectrophotometer fitted with a CryoIndustries magneto-cryostat. Spectra were collected in the Faraday configuration in fields ranging from 0 to 6 T at 5 K.

III. RESULTS AND DISCUSSION

A. Film composition

Analysis and modeling of RBS data showed that a significant degree of Co substitution is achievable by plasma-enhanced MOCVD. Figure 1 shows RBS data (circles) and a simulated spectrum (solid line) for an epitaxial $Co_xZn_{1-x}O$ film grown on $Al_2O_3(012)$. Fitting to the model, which was generated using the SIMNRA software,[14,15] reveals that $x=0.35$ for this film. Assuming that the incorporation of Co into the ZnO lattice does not significantly change the density of ZnO(5.67 g/cm^3), we estimate the thickness of this film to be 434 Å using the RBS simulation. We have also measured the thickness of the film from the fringes in the XRD reflectometry profile[16] and find that the thickness measured in this way is only 3% different than the value determined by RBS.

The growth rate is between 65 and 75 Å/min at the typical growth temperature of 748 K. This rate appears to be faster than the average growth rate (10–20 Å/min) of the $Co_xZn_{1-x}O$ material grown by pulsed laser deposition (PLD),[9] but it is actually many orders of magnitude slower than the *instantaneous* growth rate per laser pulse, which has been shown to be up to 10^6 times faster than the rate in other synthesis techniques.[17]

The Co concentration in the films depends not only on the amount of Co precursor delivered to the reactor, but also on the deposition temperature. We find that increasing the substrate temperature increases the reactivity of the Co metal-organic source relative to the Zn source. Previously it was reported that both thermal decomposition and oxidation of the precursor molecules occur in MOCVD growth using β-diketonate type sources.[18] However, at higher temperatures, thermal decomposition is dominant. From our results, it appears that above ~798 K the rate of thermal decomposition of the Co precursor molecules is notably greater than that of the Zn precursor molecule. We have also characterized the film composition as a function of thickness with SIMS depth profiling. Figure 2 shows a plot of the Zn, Co, and Al ion currents normalized to the total ion current as a function of sputter time for an Al-doped (~1 at. %) $Co_{0.09}Zn_{0.91}O$ film that has been vacuum annealed as described in the experimental section. Normalization by the total ion current partially removes matrix sensitivity effects which change as the interface is approached during sputtering. Figure 2 is also representative of data acquired on most of the as-grown films. The film-substrate interface is marked by the rapid increase in the Al counts at approximately 900 s. The fact that the profiles are very flat indicates that the Co and Al are uniformly distributed throughout the film and that very little, if any, segregation exists at the surface. This

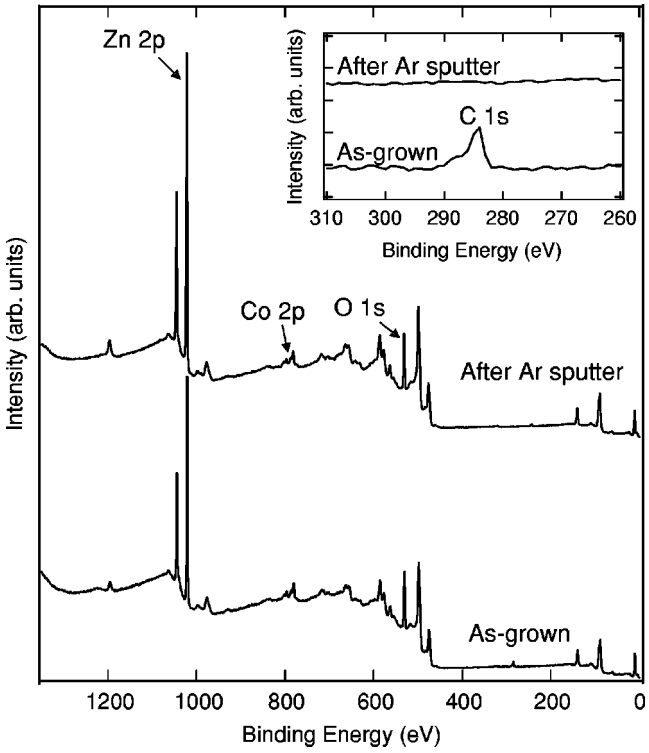

FIG. 3. XPS spectra for an Al:$Co_xZn_{1-x}O$ sample obtained before and after removal of 50 Å of surface material by sputtering. The inset shows an expanded region around the C 1*s* peak.

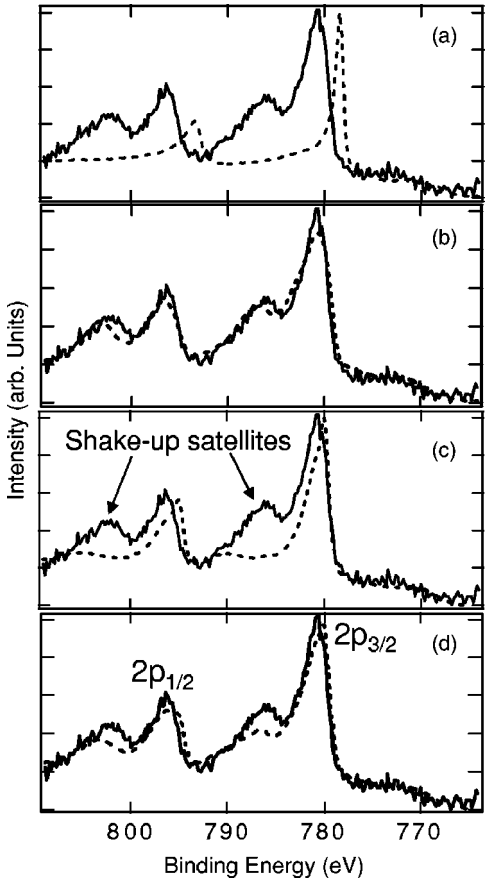

FIG. 4. Comparison of the Co 2*p* core-level photoemission line shapes for an Al-doped $Co_{0.1}Zn_{0.9}O$ film (solid line) with (a) a polycrystalline Co metal film (Co^0) grown on Si(001), (b) an epitaxial CoO film (Co^{+2}) grown on MgO(001), (c) an epitaxial γ-Co_2O_3 film (Co^{+3}) grown on MgO(001), and (d) a summation of the spectra from (b) and (c) that simulates a film containing equal concentrations of Co^{2+} and Co^{3+}.

is an important result as it shows the annealing does not induce any detectable enrichment or segregation of the Co or Al. The increase in Co and Zn signals at the interface (~900 s) is attributed primarily to changes in the ion yields at the interface not removed by normalization by the total ion current, a commonly encountered SIMS phenomenon.

Figure 3 shows XPS spectra for an Al:$Co_xZn_{1-x}O$ sample obtained on the as-grown film and after removal of 50 Å of surface material by sputtering. The inset highlights the region of the survey scan in the vicinity of the C 1*s* peak at 283 eV. The absence of the carbon peak in the spectrum obtained after sputtering indicates that the bulk of the film is free of carbon contamination. This result reveals that the metal-organic precursor molecules react completely and that the carbon-containing ligands are desorbing from the surface. The peak in the as-grown spectrum is presumably due to adsorption of adventitious hydrocarbons during sample transfer through air.

XPS was also used to characterize the charge state of the Co ions in the films. This information is useful in determining the magnetic and electrical properties of the material. Figure 4 compares the Co2*p* core level photoemission spectrum from an Al-doped $Co_{0.1}Zn_{0.9}O$ film (solid line) with spectra from various standards that contain Co atoms in different oxidation states (dashed lines). The standards consist of: (a) A polycrystalline Co metal film (Co^0) grown on Si(001), (b) an epitaxial CoO film (Co^{2+}) grown on MgO(001), (c) an epitaxial γ-Co_2O_3 film (Co^{3+}) grown on MgO(001), and (d) a linear combination of the spectra for CoO and γ-Co_2O_3 that simulates a film containing equal concentrations of Co^{2+} and Co^{3+}. Each of the standards was synthesized by molecular beam epitaxy (MBE) and then characterized by *in situ* XPS. In each case, the spectra were independently shifted such that the O 1*s* peak was positioned at a binding energy of 530.1 eV.

Comparison of the shapes and positions of the primary and satellite peaks shows that there is a good fit between the $Co_{0.1}Zn_{0.9}O$ film and the Co^{2+}standard [Fig. 4(b)] but a very poor fit to the Co^{3+} [Fig. 4(c)] and the Co^0 [Fig. 4(a)] standards. There is also poor agreement between the spectra shown in Fig. 4(d), which reveals that there is not a mixture of Co^{+2} and Co^{+3}. We, therefore, conclude that Co in our MOCVD-grown films is in the +2 oxidation state. It is expected that Co^{+2} would incorporate into the wurtzite lattice at Zn^{+2} sites since the ionic radii of four-coordinate Zn^{+2} and Co^{+2} (0.060 and 0.066 nm, respectively) differ by only 10% and Co^{+2} is very soluble in ZnO.[19] Thus, within the detection limits of the spectrometer, we can rule out metallic Co as the observed source of ferromagnetism.

B. Film structure and surface morphology

XRD patterns reveal that all $Co_xZn_{1-x}O$ films on sapphire were crystalline. However, the nature of the crystallinity (i.e.,

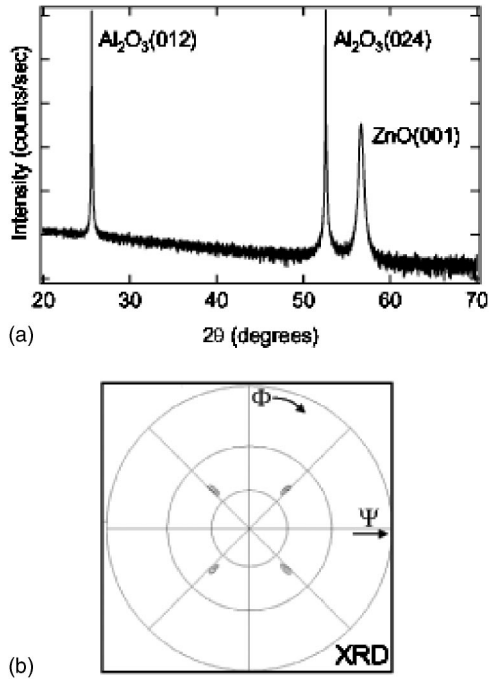

FIG. 5. XRD results for a $Co_{0.1}Zn_{0.9}O$ film grown at 475 °C. Part (a) shows a θ-2θ scan and (b) shows a pole figure of the same sample.

single-crystal, highly oriented, or randomly oriented) depends strongly on both the Co content and the growth temperature. Epitaxial growth of $Co_xZn_{1-x}O$ films is possible for $0<x<0.35$ between 723 and 798 K. However, if the Co concentration is increased by injecting a greater volume of Co precursor or by increasing the growth temperature (as high as 873 K), the resultant films are typically polycrystalline and highly (110) or (001) oriented. Separate CoO is seen if the temperature and/or Co concentration is further increased.

Figure 5(a) shows the XRD pattern for a $Co_{0.1}Zn_{0.9}O$ film grown at 748 K. The single ZnO(110) peak at 55.806° indicates that the film is highly (110) oriented, if not single crystalline. The absence of crystalline metallic Co or CoO_x suggests that the film is single phase. Furthermore, from the ZnO(110) peak position, we calculate the lattice parameter, *a*, to be 3.291 Å. This value is 1.3% larger than that of pure wurtzite ZnO (3.250 Å) and is most likely due to the substitution of the larger Co^{+2} ion for Zn^{+2}.

In order to determine whether the film was single-crystalline or highly oriented, we acquired an XRD pole figure using a four-circle diffractometer, which can reveal information regarding in-plane crystallinity.[20] In the pole figure shown in Fig. 5(b), the ZnO(101) diffraction peaks from a $Co_{0.1}Zn_{0.9}O$ film are shown as a contour plot. The sample tilt, Ψ, is the angle by which the surface is tilted out of the diffraction plane. In the figure, Ψ increases linearly in the radial direction from 0° to 90° and the three concentric rings represent Ψ values of 30°, 60°, and 90°. The angle of rotation about the surface normal is denoted by Φ, which ranges from 0° to 360°. In the plot, Φ varies around the circumference of the circle and each radial line represents a Φ increment of 45°. As expected for an epitaxially grown $Co_xZn_{1-x}O(110)$ film, the pole figure shows four diffraction spots at $\Psi=40°$. If, instead, the film were only oriented and had in-plane randomness, the pole figure would be characterized by a ring at $\Psi=40°$. Finally, our results are in agreement with Liu *et al.* who show that the following epitaxial relationship exists for ZnO on *r*-plane sapphire.[21]

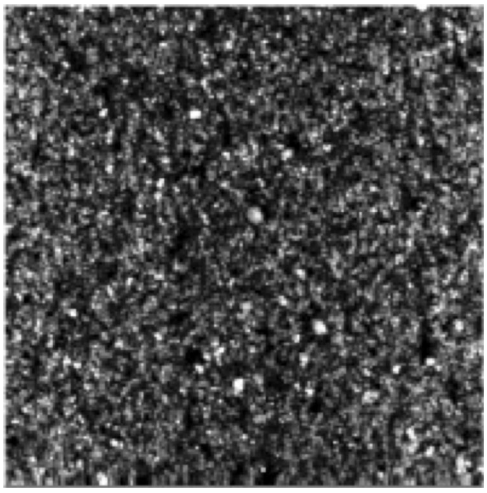

FIG. 6. AFM micrograph of a 530 nm thick $Co_{0.1}Zn_{0.9}O$ film. This is the same sample for which XRD data is shown in Fig. 5. The lateral dimensions are 5 μm × 5 μm and the vertical relief is 20 nm.

$$\mathrm{ZnO}(110)\|\mathrm{Al_2O_3}(012) \text{ and } \mathrm{ZnO}[001]\|\mathrm{Al_2O_3}[011]. \quad (2)$$

The surface morphology of the $Co_xZn_{1-x}O$ films was characterized using AFM. Figure 6 shows a micrograph of the surface of a 530 nm thick $Co_{0.1}Zn_{0.9}O$ film grown at 748 K [same film as in Fig. 5(a)]. The film consists of dense and fairly uniformly sized grains that are roughly 100 nm in diameter. The existence of these small grains indicates that the nucleation density was rather high and that the growth proceeded in a three-dimensional fashion. Furthermore, since the pole figure in Fig. 5(a) shows that this film is epitaxial, each of the grains remained in registry with the substrate during film growth.

C. Electrical and magnetic properties

The influence of annealing on the resistivity was investigated for several Al-doped $Co_xZn_{1-x}O$ films that were similarly grown. Prior to annealing and in spite of the intentional *n*-type doping with 1% aluminum, the films were highly resistive. As a result of the vacuum anneal, the resistivity typically decreased from >10 to $\sim 0.01\ \Omega\cdot$cm. We believe that this change in resistivity is caused by the generation of oxygen vacancies due to the reductive nature of the vacuum anneal. This conclusion is supported by Chang *et al.* who show that annealing ZnO films in a hydrogen atmosphere results in a decrease in resistance, while annealing in air results in a dramatic increase in resistance.[22] They conclude that annealing in any type of oxidizing atmosphere not only eliminates oxygen vacancies, but can also incorporate addi-

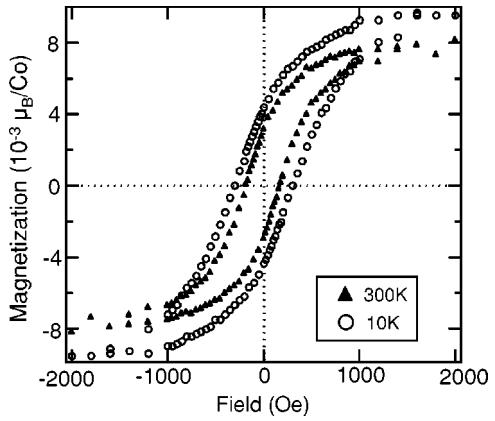

FIG. 7. SQUID-derived hysteresis loop acquired on a an Al-doped $Co_xZn_{1-x}O$ film measured at 10 and 300 K, where $x = 0.09$.

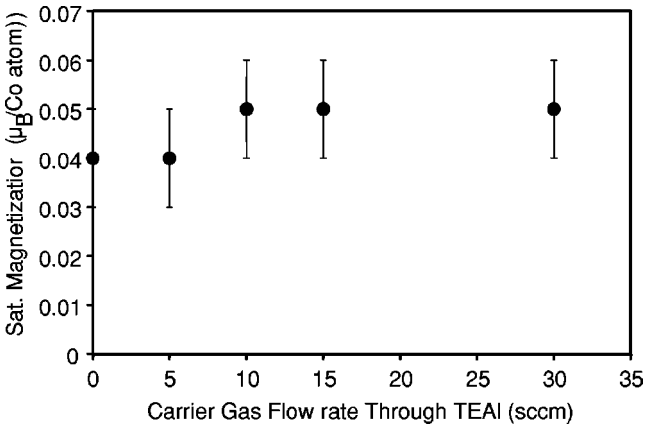

FIG. 8. A plot of the room-temperature saturation moment as a function of the Al concentration in various $Co_{0.1}Zn_{0.9}O$ films after vacuum annealing.

tional oxygen along grain boundaries, thereby reducing the carrier concentration. Interestingly, the fact that the fully oxidized, Al-doped $Co_xZn_{1-x}O$ films were resistive suggests that the O-vacancies generated during the anneal, and not the Al dopant, are the source of free carriers. Most likely, impurity atoms such as carbon and hydrogen passivate the Al atoms and prevent the Al from acting as an electron donor. Hall effect and resistance measurements on annealed $Co_xZn_{1-x}O$ films without Al doping show resistivities of approximately $2\times10^{-3}\Omega\cdot$cm with an electron carrier concentration of $\sim2.2\times10^{20}$ cm^{-3} and provide further evidence that impurity dopants are not necessary to achieve *n*-type conduction in ZnO-based materials.

Room-temperature magnetic measurements on the VSM were performed on films of thickness in the range 200–600 nm deposited on 1×1 cm^2 substrates. For SQUID measurements samples were cut to 1×0.5 cm^2 dimensions. SQUID scans on the as-grown samples, measured at 2, 5, and 10 K, show a combination of paramagnetic and diamagnetic behavior, the latter being due to the substrate. However, the vacuum annealed $Co_xZn_{1-x}O$ films consistently demonstrated weak ferromagnetic behavior. The saturation magnetization was observed to increase with conductivity, which in turn depended on the details of the post-growth vacuum anneal. The value of spontaneous moment per Co atom at room temperature ranged from 0.01 to 0.07 μ_B per Co, coercive fields were in the range 100–200 Oe. Figure 7 shows M–H hysteresis loops for a vacuum-annealed, Al-doped $Co_{0.09}Zn_{0.91}O$ film measured at 10 and 300 K. The measured magnetization has been compensated for the diamagnetic background and then scaled to units of μ_B per Co atom. At 10 K, the coercive field, H_c, is 300 Oe, while the saturation magnetization, M_s, is only 0.01 μ_B per Co atom in this particular sample. At 300 K, the M_s and H_c values are smaller; however, hysteresis is still clearly observed. Similar results were found for Co concentrations up to 34%, where the saturation moment and coercivity, at room temperature, were found to be 0.07 μ_B per Co atom and 100 Oe, respectively. The rather small value for saturation magnetization suggests that only a small portion of Co spins are coupled ferromagnetically and that a significant paramagnetic fraction of Co remains.

The dependence of the magnetic properties on resistivity is presumably a result of the generation of carriers during the vacuum anneal and is consistent with the model of carrier-induced ferromagnetism. However, the carriers do not originate from their intended source—the Al dopant atoms. Figure 8 shows the room-temperature saturation moment, determined by VSM, as a function of the Al concentration in various $Co_{0.1}Zn_{0.9}O$ films after vacuum annealing. In the figure, we represent the Al content, which ranges from 0 at % to roughly 1.5 at %, by the carrier gas flow rate through the triethylaluminum source bubbler. If the carriers responsible for mediating the magnetic behavior in the films were associated with the Al dopant, one would expect the saturation moment to decrease to zero with decreasing Al concentration. However, within the experimental error, the magnetization is independent of the Al content, indicating that Al is not responsible for the conductivity.

Figure 9 displays both the temperature dependence of the saturation moment, measured from 10 to 350 K at a field of 2000 Oe, and the remanence, measured at zero field, for another $Co_{0.09}Zn_{0.91}O$ film. The saturation moment versus temperature plot was obtained by first subtracting out the diamagnetic background, which also contained the

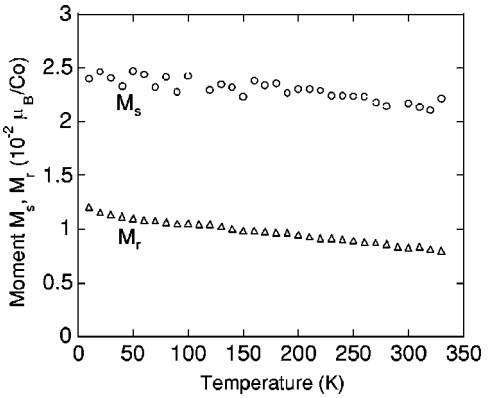

FIG. 9. Plots of both the temperature dependence of the saturation moment, measured from 10 to 350 K at a field of 2000 Oe, and the remanence, measured at zero field.

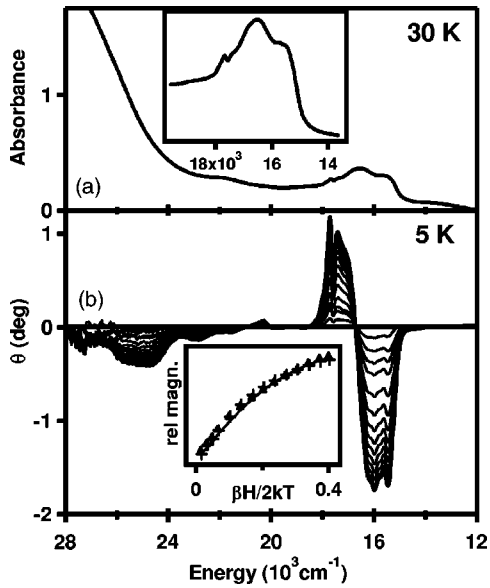

FIG. 10. (a) 30 K absorption and (b) 5 K, 0 to 6 T variable-field MCD spectra of a MOCVD-grown $Co_{0.09}Zn_{0.91}O$ thin film where θ is the ellipticity. The inset in part (a) shows an expanded view of the spectra between 15 000 and 19 000 cm^{-1}. The inset in part (b) shows the 5 K saturation magnetization at 24 727 cm^{-1} and 15 465 cm^{-1} with the solid line showing the $S=3/2$ Brillouin function calculated for $g=2.25$.

paramagnetic contribution, from the magnetization value measured at each temperature, and then smoothing the data using a three-point boxcar algorithm. Both the saturation remanent magnetizations, although weak, decrease very gradually and do not exhibit a region of rapid decline up to 350 K, indicating that the Curie temperature is greater than 350 K.

Figure 10 shows the 30 K absorption and 5 K variable-field MCD spectra of a $Co_{0.09}Zn_{0.91}O$ thin film sample. The absorption and MCD spectra in the bandgap region could not be measured because of the large sample thickness ($\sim$300 nm). The structured absorption band in the range of $15,000-19,000$ cm^{-1}, shown in the inset of Fig. 10(a), arises from the spin-orbit split $^4A_2(F)\rightarrow{}^4T_1(P)$ ligand-field transition of tetrahedral d^7 Co^{2+} with additional contributions from the numerous nearby doublet levels, as discussed in detail previously.[23,24] The similarity of the ligand-field absorption spectrum in Fig. 10(a) to those of the bulk single crystal samples clearly demonstrates substitutional Co^{2+} doping in this ZnO film.[23,24] This optical assignment of oxidation state is consistent with the XPS data in Fig. 4.

The fine structure of the C-term MCD feature between 15 000 and 19 000 cm^{-1} again reflects the spin-orbit splitting of the $^4T_1(P)$ excited state. The very sharp interference dip at 17 575 cm^{-1} correlates with a weaker dip in the absorption spectrum. We interpret this dip as resulting from a Fano-type anti-resonance involving interaction of the $^2A_1(G)$ and $^4T_1(P)$ excited states. This effect has been well documented in octahedral Cr^{3+} sites[25,26] possessing the $^4A_2(F)$ ground state but is rarely observed in the spectra of tetrahedral Co^{2+} ions.[24,27] The inset in Fig. 10(b) shows the 5 K saturation magnetization behavior of the MCD intensities measured at 24 727 and 15 465 cm^{-1}. The solid line shows the $S=3/2$ Brillouin function calculated for $g=2.25$.[28] Deviation of the experimental curves from the Brillouin function is due to the +5.5 cm^{-1} zero-field splitting of the $^4A_2$ ground state[24] that is not accounted for in the Brillouin function, which assumes a pure spin multiplet. A detailed analysis of the low-temperature MCD saturation magnetization nesting behavior in Co^{2+}-doped ZnO is beyond the scope of this paper but is reported elsewhere.[29] These MCD saturation magnetization data demonstrate that the majority of the Co^{2+} ions in this sample behave as magnetically isolated $S=3/2$ ions.

TABLE II. C_0/D_0 ratios for five prominent features.

Band (cm^{-1})	C_0/D_0
15 448	−0.25
15 984	−0.25
17 427	+0.20
17 708	+0.26
24 727	−0.05

An attempt was made to detect the ferromagnetic species using MCD spectroscopy performed at high temperatures. Whereas the paramagnetic magnetization diminishes with increasing temperature approximately following Curie behavior, that of the ferromagnetic species does not (Fig. 7). No MCD signal attributable to a ferromagnetic species was detectable. The ferromagnetic behavior shown in Fig. 7 must, therefore, arise from a minor fraction of the cobalt ions present in this sample, indicating the presence of two types of magnetic cobalt species. This interpretation is in agreement with the saturation limit of the ferromagnetic magnetization, the magnitude of which is approximately 1% of the expected total saturation moment per high-spin $Co^{2+}(3\mu_B)$.

In addition to the ligand field transitions centered at 17 000 cm^{-1}, a second MCD feature is observed at $\sim$24 700 cm^{-1} that corresponds to the broad featureless bandgap onset in the absorption spectrum. As shown in the inset of Fig. 10(b), this negative MCD feature also exhibits $S=3/2$ saturation magnetization behavior, revealing that it also derives from tetrahedral Co^{2+} ions. This transition has been assigned previously as a charge transfer (CT) transition involving the Co^{2+} ions (*vide infra*).[30] The assignment of this feature as a CT transition is supported by analysis of its C_0/D_0 ratio, defined as[31]

$$C_0/D_0 = kT/\beta H(\Delta\varepsilon/\varepsilon), \tag{3}$$

where $k=0.695\,03$ cm^{-1}/K, T is the temperature (K), β is 0.466 86 $cm^{-1}/Tesla$, H is the applied field (Tesla), $\Delta\varepsilon$ is the molar ellipticity, and ε is the molar absorption coefficient. The C_0/D_0 ratio thus parametrizes the MCD intensity relative to the absorption intensity for a given transition. C_0/D_0 ratios for four prominent features are presented in Table II. Experimentally, the C_0/D_0 ratio, is typically as much as an order of magnitude lower for CT transitions than for ligand-field bands in sites of reduced symmetry due to the greater

spin-orbit coupling strength of the metal.[32] The values shown in Table II are thus consistent with the assignment of the negative MCD intensity and the broad tailing absorption intensity at 24 727 cm^{-1} as due to a CT transition. Because of overlap with the bandgap onset, the MCD feature observed maximizes at lower energy and has a truncated bandshape on the high-energy side, and therefore, provides a lower limit for the energy of this transition. Consequently, the absorption and MCD intensities of this CT transition are difficult to measure reliably, and the C_0/D_0 value for this transition reported in Table II is considered approximate.

We now address the specific nature of this CT transition in Co^{2+}-doped ZnO. It has previously been assigned as a metal-to-ligand charge transfer (MLCT) transition involving promotion of a Co^{2+} *d* electron into the ZnO conduction band.[30] Its assignment, however, as a ligand-to-metal charge transfer (LMCT) transition in which a valence band electron is promoted into a Co^{2+} *d* orbital, is also possible. Although these two classes of CT transitions may in fact both occur in the same energy region,[33] we prefer to assign the absorption and negative MCD intensity in this region as arising from a LMCT transition. This assignment is based on orbital overlap considerations and comparison to Ni^{2+}-doped ZnO. A sub-band gap LMCT transition having an absorption edge at ~19 655 cm^{-1} has been identified in bulk Ni^{2+}-doped ZnO and recently in Ni^{2+}-doped ZnO nanocrystals.[23,34,35] Using Jørgensen's optical electronegativity model[36] and the well-characterized optical electronegativities of tetrahedral Co^{2+}(1.9) and Ni^{2+}(2.05),[37] the analogous LMCT transition in Co^{2+}-doped ZnO is predicted to occur ~8000 cm^{-1} to higher energy,[29] in the energy region where this intensity is observed experimentally in Fig. 10. It is important to note that, whereas the optical electronegativity model was developed for discrete metal-ligand bonded pairs, the LMCT process in Co^{2+}-doped ZnO involves promotion of a valence electron into a Co^{2+}-localized *d* orbital. The initially prepared excited state thus involves a loosely bound hole in the valence level coupled to the reduced dopant,[38] and differs substantially from the corresponding excitation anticipated for molecular oxyanion complexes.

Assignment of the sub-bandgap absorption and negative MCD charge-transfer intensity in $Co_xZn_{1-x}O$ as arising from an LMCT transition is further supported by orbital overlap considerations. In the general case, the intensity of a CT transition is governed by covalent mixing of the donor and acceptor wave functions as described by Eq. (4)

$$\phi_A' = \sqrt{1-c^2}(\phi_A) - c\phi_D, \tag{4}$$

where ϕ_A and ϕ_D are the unperturbed one electron orbitals of the CT acceptor and donor, respectively. Both theoretical and experimental studies indicate the donor-acceptor CT intensity is proportional to the square of the mixing coefficient, *c*:[32]

$$I_{CT} \propto c^2, \tag{5}$$

where *c* is proportional to the donor-acceptor resonance integral and inversely proportional to the mismatch in valence-shell ionization energies, E_A and E_D:

$$c \approx \frac{-[\int \phi_A H \phi_D d\tau]}{E_A - E_D}. \tag{6}$$

The *p-d* hybridization in II–VI semiconductors that gives rise to LMCT intensity is generally over an order of magnitude greater than *s-d* hybridization responsible for MLCT intensity, and the charge transfer intensity will, therefore, be dominated by the former.

The observation of a sub-band gap CT feature is of interest in the area of spintronics because it relates to delocalization of spin from the dopant ion into the semiconductor band structure. The observation of a sub-bandgap CT transition in $Co_xZn_{1-x}O$ reveals a relatively small denominator in Eq. (6) that favors hybridization of Co^{2+} and ZnO wave functions. Hybridization is also favored by the small unit cell dimensions of ZnO ($a=3.2495$ Å, $c=5.2067$ Å), since the resonance integral in Eq. (6) is proportional to orbital overlap. This *p-d* covalency is directly responsible for the unique magnetic and magneto-optical properties of DMSs in general,[39] and in particular its magnitude has been identified as a key factor in determining T_C in ferromagnetic DMSs.[10]

IV. CONCLUSIONS

We have grown epitaxial $Co_xZn_{1-x}O(110)$ on $Al_2O_3(012)$ by plasma enhanced metalorganic chemical vapor deposition using a liquid-precursor delivery system. We find that large amounts of Co ($x \leqslant 0.35$) can be uniformly incorporated into the film without phase segregation. The Co appears to substitute for tetrahedrally coordinated Zn cations in the lattice and exhibits a +2 oxidation state. There is no evidence for the formation of either metallic Co or CoO_x particles in the thin film. Prior to annealing and in spite of the *n*-type doping with Al, the as-grown films were highly resistive. It appears that oxygen vacancies generated during the vacuum anneal, rather than Al dopants, contribute the majority of the carriers. Furthermore, all the films that were annealed showed weak ferromagnetic behavior up to 350 K, which is the highest temperature measured to date. Finally, using low-temperature optical absorption and MCD spectroscopies we have identified a sub-bandgap transition that we assign as a ZnO valence band to Co^{2+} *d* orbital ligand-to-metal charge transfer transition. The relatively low energy of this transition, combined with the small unit cell dimensions of ZnO, favors Co^{2+}-ZnO *p-d* covalency and likely contributes to the high Curie temperature for ferromagnetism in this DMS.

ACKNOWLEDGMENTS

The work at PNNL was performed in the Environmental Molecular Sciences Laboratory, a national scientific user facility sponsored by the Department of Energy's Office of Biological and Environmental Research and located at Pacific Northwest National Laboratory. This work was supported by the PNNL Nanoscience and Technology Initiative, the U. S. Department of Energy, Office of Science, Office of

Basic Energy Sciences, Division of Materials Science, and the DARPA Spins in Semiconductors Initiative. A. C. T. and J. D. B. acknowledges support from the Joint Institute for Nanoscience funded by the Pacific Northwest National Laboratory (operated by Battelle for the U. S. Department of Energy) and the University of Washington. Funding from the NSF (ECS-0224138 to K.M.K., S.A.C., and D.R.G.) is gratefully acknowledged.

*Corresponding author.

[1] G. Burkard, H.-A. Engel, and D. Loss, Fortschr. Phys. **48**, 965 (2000).
[2] D. Loss and D. P. Vincenzo, Phys. Rev. A **57**, 120 (1998).
[3] A. Hirohata, Y. B. Xu, C. M. Guertler, and J. A. C. Bland, J. Appl. Phys. **85**, 5804 (1999).
[4] A. T. Hanbicki, G. T. Jonker, G. Itskos, G. Kioseoglou, and A. Petrou, Appl. Phys. Lett. **80**, 1240 (2002).
[5] R. Fiederling, M. Keim, G. Reuscher, W. Ossau, G. Schmidt, A. M. Waag, and L. W. Molenkamp, Nature (London) **402**, 787 (1999).
[6] B. T. Jonker, Y. D. Park, B. R. Bennett, H.-D. Cheong, G. Kioseoglou, and A. Petrou, Phys. Rev. B **62**, 8180 (2000).
[7] M. L. Reed, N. A. El-Masry, H. H. Stadelmaier, M. K. Ritums, M. J. Reed, C. A. Parker, J. C. Roberts, and S. M. Bedair, Appl. Phys. Lett. **79**, 3473 (2001).
[8] Y. Matsumoto, M. Murakami, T. Shono, T. Hasegawa, T. Fukumura, M. Kawasaki, P. Ahmet, T. Chikyow, S.-Y. Koshihara, and H. Koinuma, Science **291**, 854 (2001).
[9] K. Ueda, H. Tabata, and T. Kawai, Appl. Phys. Lett. **79**, 988 (2001).
[10] T. Dietl, H. Ohno, F. Matsukura, J. Cibert, and D. Ferrand, Science **287**, 1019 (2000).
[11] D. P. Norton, S. J. Pearton, A. F. Hebard, N. Theodoropoulou, L. A. Boatner, and R. G. Wilson, Appl. Phys. Lett. **82**, 239 (2003).
[12] K. Sato and H. Katayama-Yoshida, Jpn. J. Appl. Phys., Part 2 **40**, L334 (2001).
[13] T. F. Kaech, D. J. Wolford, E. Veohoff, V. Deline, P. M. Mooney, R. Potemski, and J. Bradly, J. Appl. Phys. **62**, 632 (1987).
[14] M. Matej (Max Planck Institute, Garching, Germany, 1997).
[15] W. Eckstein and M. Mayer, Nucl. Instrum. Methods Phys. Res. B **153**, 337 (1999).
[16] P. F. Fewster, *X-ray Scattering from Semiconductors* (Imperial College Press, London, 2000).
[17] H.-U. Krebs, O. Bremert, M. Stormer, and Y. Luo, Appl. Surf. Sci. **86**, 90 (1995).
[18] Y. Gao, S. He, P. Alluri, M. Engelhard, A. S. Lea, J. Finder, B. Melnick, and R. L. Hance, J. Appl. Phys. **87**, 124 (2000).
[19] Z. Jin, M. Murakami, T. Fukumura, Y. Matsumoto, A. Ohtomo, M. Kawasaki, and H. Koinuma, J. Cryst. Growth **214/215**, 55 (2000).
[20] P. A. Stampe and R. J. Kennedy, J. Cryst. Growth **191**, 478 (1998).
[21] Y. Liu, C. R. Gorla, S. Liang, N. Emanetoglu, Y. Lu, H. Shen, and M. Wraback, J. Electron. Mater. **29**, 69 (2000).
[22] J. F. Chang, W. C. Lin, and M. H. Hon, Appl. Surf. Sci. **183**, 18 (2001).
[23] H. A. Weakliem, J. Chem. Phys. **36**, 2117 (1962).
[24] P. Koidl, Phys. Rev. B **15**, 2493 (1977).
[25] R. Schenker, M. Triest, C. Reber, and H. U. Guedel, Inorg. Chem. **40**, 5787 (2001).
[26] A. Lempicki, L. Andrews, S. J. Nettel, B. C. McCollum, and E. I. Solomon, Phys. Rev. Lett. **44**, 1234 (1980).
[27] J. F. Donegan, F. G. Anderson, F. J. Bergin, T. J. Glynn, and G. F. Imbusch, Phys. Rev. B **45**, 563 (1992).
[28] W. H. Brumage, C. F. Dorman, and C. R. Quade, Phys. Rev. B **63**, 104411 (2001).
[29] D. Schwartz, N. S. Norberg, Q. Nguyen, J. Parker, and D. R. Gamelin, J. Am. Chem. Soc. **125**, 13205 (2003).
[30] Z.-W. Jin, T. Fukumura, K. Hasegawa, Y. Z. Yoo, K. Ando, T. Sekiguchi, P. Ahmet, T. Chikyow, T. Hasegawa, H. Koinuma, and M. Kawasaki, J. Cryst. Growth **237-239**, 548 (2002).
[31] S. B. Piepho and P. N. Schatz, *Group Theory in Spectroscopy with Applications to Magnetic Circular Dichroism* (Wiley, New York, 1983).
[32] E. I. Solomon and A. B. P. Lever, *Inorganic Electronic Structure and Spectroscopy* (Wiley, New York, 1999).
[33] J. Dreyhsig, J. Phys. Chem. Solids **59**, 31 (1998).
[34] J. M. Noras and J. W. Allen, J. Phys. C **13**, 3511 (1980).
[35] P. V. Radovanovic, N. S. Norberg, K. E. McNally, and D. R. Gamelin, J. Am. Chem. Soc. **124**, 15192 (2002).
[36] C. K. Jorgensen, *Orbitals in Atoms and Molecules* (Academic, New York, 1962).
[37] A. B. P. Lever, *Inorganic Electronic Spectroscopy* (Elsevier, Amsterdam, New York, 1968).
[38] R. Heitz, A. Hoffmann, and I. Broser, Phys. Rev. B **48**, 8672 (1993).
[39] J. K. Furdyna, J. Kossut, and Editors, *Semiconductors and Semimetals, Vol. 25: Diluted Magnetic Semiconductors*, 1988.